Title Page

IRGM/Irgm1 Aggravates Progression of Atherosclerosis by Inducing Macrophage Apoptosis through the MAPK Signaling Pathway

Running Title: IRGM/Irgm1-induced Macrophage Apoptosis Aggravates Atherosclerosis

Shaohong Fang[1,2†], Song Sun[2,3†], Hengxuan Cai[1,2†], Xinran Hao[2,3], Xiaoyi Zou[2,3], Xin Wan[2,3], Jiangtian Tian[1,2], Zhaoying Li[1,2], Shanjie Wang[1,2], Zhongze He[2,3], Wei Huang[2,3], Chenchen Liang[1,2], Zhenming Zhang[1,2], Liming Yang[4], Jinwei Tian[1,2*], Bo Yu[1,2*] and Bo Sun[2,3*]

[1]Department of Cardiology, Second Affiliated Hospital of Harbin Medical University, Harbin 150086, China;

[2]The Key Laboratory of Myocardial Ischemia, Chinese Ministry of Education, Harbin 150086, China;

[3]Department of Neurobiology, Harbin Medical University; Neurobiology Key Laboratory, Education Department of Heilongjiang Province, Harbin 150086, China;

[4]Department of Pathophysiology, Harbin Medical University-Daqing, Daqing 163319, China

[†]The first three authors contributed equally to this article.

*Address for correspondence:

Bo Sun, 158 Baojian Road, Nangang District, 150086 Harbin, China. Tel: +86 451 8827 2363, Fax: +86 451 8827 2363, Email: sunbohmu@163.com;

Bo Yu, 246 Xuefu Road, Nangang District, 150086 Harbin, China. Tel: +86 451 8660 5180, Fax: +86 451 8660 5180, Email: dryu_hmu@163.com;

Jinwei Tian, 246 Xuefu Road, Nangang District, 150086 Harbin, China. Tel: +86 451 8660 5800, Fax: +86 451 8660 5800, Email: tianjinweidr2009@163.com.

Word count: 8904

The authors have declared that no conflict of interest exists.

Abstract

Aims

Atherosclerosis underlies most cardiovascular diseases, among which acute coronary syndrome (ACS) caused by plaque rupture (PR) often leads to death. Immune-related GTPases (IRGM/Irgm1) have been extensively studied in inflammatory diseases, but their role in atherosclerosis is unclear. Determining how IRGM/Irgm1 promotes atherosclerotic plaque vulnerability will provide information for new biomarkers and/or therapeutic targets.

Methods and results

We identified ruptured and unruptured plaques by optical coherence tomography, and found that serum IRGM was highly expressed in patients with ST-segment elevation myocardial infarction in PR. We used ApoE$^{-/-}$Irgm1$^{+/+}$, ApoE$^{-/-}$Irgm1$^{+/-}$ mice and chimeric mice to establish a model of advanced atherosclerosis. The results of pathological experiments showed that Irgm1 caused plaque necrosis. The ratio of neutral lipids and cholesterol crystals increases, while the content of collagen fibers decreases, aggravating the destabilization of atherosclerotic plaques. In vitro, we used multiple approaches to confirm that Irgm1 promotes macrophage apoptosis by promoting the production of reactive oxygen species and activating the MAPK signaling pathway.

Conclusions

IRGM may be a potential risk factor for PR. Mechanistic studies have shown that IRGM/Irgm1 contributes to the formation and rupture of fragile plaques. This is partly mediated by the induction of macrophage apoptosis via the MAPK signaling pathway. IRGM may offer new strategies for early treatment of ACS.

Translation view

Our findings indicate that IRGM/Irgm1 contributes to formation and rupture of vulnerable plaques. It suggests that IRGM may provide a new target for the early treatment of ACS.

Introduction

Acute coronary syndrome (ACS), the main complication of atherosclerosis, is the commonest cause of morbidity and mortality worldwide (1). Three main pathological mechanisms lead to ACS: plaque rupture (PR), plaque erosion (PE), and calcified nodules (CN) (2, 3). Historically, research on pathological mechanisms of ACS has mostly relied on autopsy (4). Today, intracoronary optical coherence tomography (OCT) makes it possible to identify the plaque morphologies of patients *in vivo* and probe the pathogenesis of atherosclerotic plaque progression (5). Previously, we used OCT to assess distribution of culprit plaque in ACS patients and confirmed that PR has the highest incidence among the three pathological mechanisms above (6). Vulnerable plaques with thin fibrous caps and large lipid burdens are prone to rupture (7). These findings suggest that increased plaque vulnerability is closely related to PR and the subsequent ACS, and warrants an investigation of the factors and mechanisms that influence vulnerability of plaques. Many clinical trials have suggested that age, smoking, hypertension, chronic kidney disease, and dyslipidemia are associated with plaque vulnerability (8-11). However, molecular mechanisms influencing the vulnerability of atherosclerotic plaques remain unclear.

As the primary immune cells infiltrated in atherosclerotic plaques, macrophages play vital roles in regulating plaque development and stability (18-21). Excessive

numbers of apoptotic macrophages are found in vulnerable plaques (22). Macrophage apoptosis causes plaque instability and increases risk of adverse cardiovascular events (23-25). Knowledge of upstream targets that regulate macrophage apoptosis would aid clinical assessment of the risk of vulnerable plaque formation.

The Immunity-related GTPase (IRGM in humans, Irgm1 in mice), belongs to a family of IFN-γ-inducible GTPases (12, 13). IRGM/Irgm1 acts in inflammatory bowel disease, tumors, and other diseases, yet few studies have focused on IRGM/Irgm1 in atherosclerotic disease (14, 15). Previously, we found that Irgm1 influences the progression of atherosclerotic plaques by regulating uptake of oxidized low-density lipoprotein (ox-LDL) by macrophages and the formation of foam cells (16). We have shown that IRGM/Irgm1 promotes the polarization of M1 subtype macrophages and thus aggravates the progression of atherosclerosis (17). These studies indicate that IRGM/Irgm1 expressed in macrophages can promote progression of atherosclerosis and regulate the immune response of macrophages. However, it is not known if IRGM/Irgm1 expressed in macrophages can cause plaque destabilization by affecting apoptosis.

Here, we used OCT to assess morphological features of culprit plaques in patients with ST-segment elevation myocardial infarction (STEMI), and classified patients according to the existence of PR *in vivo*. Serum studies revealed that IRGM

was highly expressed in patients with ruptured plaques (the RUP group). Expression of IRGM was correlated with PR in STEMI patients, which can thus be regarded as a potential factor contributing to PR. We clarified *in vivo* that Irgm1 was able to modify phenotype and exacerbate vulnerability of atherosclerotic plaques. Finally, we verified that Irgm1 caused plaque destabilization by promoting macrophage apoptosis. This study provides a new pleiotropic role for IRGM/Irgm1 and unveils novel potential targets for the prevention and treatment of ACS.

Results

Serum IRGM is correlated with atherosclerotic PR events in STEMI patients. Initially, we investigated whether serum Irgm1 is associated with atherosclerotic PR in STEMI patients (supplementary Figure 6). Among 85 STEMI patients with analyzable OCT images, PR was the underlying pathology in 52 subjects (61.2%). Figure 1A shows representative OCT images of normal vessels and culprit sites of plaques in RUP and NO-RUP groups. Supplemental Table 1 compares baseline clinical characteristics between RUP and NO-RUP groups. Serum LDL-C and total cholesterol (TC) levels were higher in patients with PR, while no significant differences were observed in other indicators. Plaque characteristics as assessed by OCT are presented in Supplemental Table 2. The prevalence of thin-cap fibroatheroma (TCFA) and lipid-rich plaque was higher, and minimum fibrous cap was thinner in the RUP group.

Serum IRGM was quantified by ELISA, and differed significantly among the three groups. Patients in the RUP group had the highest serum IRGM levels; healthy volunteers had the lowest (Figure 1B).

We next evaluated the ability of serum IRGM level to predict PR in patients with STEMI (Figure 1C). Without adjusting for any factors, IRGM was a strong risk factor, with an odds ratio (OR) of 1.23 (95% confidence interval (CI): 1.06~1.43, p = 0.006). As baseline characteristics differed between these two groups, we adjusted factors including age, hypertension, diabetes mellitus, current smoking, lipid factors, peak

troponin I (TnI) and high-sensitivity C-reactive protein (hs-CRP) in four different models. After each increase in the adjustment factors of the models, IRGM remains an effective predictor of PR, with an OR of 1.28 (95% CI: 1.06~1.54, p = 0.012) in model 4. Thus, serum IRGM potentially predicts atherosclerotic PR events in subjects with STEMI, independent of LDL-C and TC levels.

IRGM is highly expressed in patients with atherosclerotic plaque and positively correlated with CD68. Immunohistochemistry was used to observe the expression of IRGM and CD68 in intravascular intimal plaques. The results showed that expression of IRGM and CD68 in atherosclerotic plaques and their proportion in plaques were significantly increased (Figure 1D–1F). We analyzed the correlation between the expression of IRGM and CD68 in plaques (Supplemental Figure 2F) and found that expression of CD68 and IRGM was positively correlated. Together, these results indicated that IRGM was highly expressed in atherosclerotic plaques and mostly exists in $CD68^{+}$ macrophages within the plaques.

Irgm1 can affect atherosclerotic lesion phenotype in vivo. To investigate whether Irgm1 can affect atherosclerotic lesion phenotypes *in vivo*, we first distinguished $ApoE^{-/-}Irgm1^{+/-}$ and $ApoE^{-/-}Irgm1^{+/+}$ mice by genotypic analysis (Figure 2A). Compared with $ApoE^{-/-}Irgm1^{+/+}$ mice, Irgm1 expression was significantly reduced in

eleven major organs or cell types of ApoE$^{-/-}$Irgm1$^{+/-}$ mice (Supplemental Figure 3A). After a Western diet for 16 weeks, mice aorta showed positive oil-red O (ORO) staining, a hallmark of atherosclerotic lesions (Figure 2B-C). There was no difference in the positive area of the aortic arch between two groups, while the positive areas in both the thoracic and abdominal parts were significantly reduced in the ApoE$^{-/-}$Irgm1$^{+/-}$ group (Supplemental Figure 3B). The percentage of ORO positive areas in the aortic lumen area in the aortic arch, thoracic aorta, and abdominal aorta in ApoE$^{-/-}$Irgm1$^{+/-}$ mice were significantly reduced (Figure 2C–D). As shown by H&E staining (Figure 2E), ApoE$^{-/-}$ Irgm1$^{+/-}$ mice had a thicker fibrous cap, reduced necrotic core area and necrotic core ratio, although there was no significant difference in lesion areas between the two groups (Figure 2F–G, 2J; Supplemental Figure 3C). Next, we observed the content of neutral lipids in the aortic sinus of mice by ORO staining. We found that the content and percentage of neutral lipids in ApoE$^{-/-}$Irgm1$^{+/-}$ mice were significantly lower than those in ApoE$^{-/-}$Irgm1$^{+/+}$ mice (Figure 2H, 2K; Supplemental Figure 3E). Masson staining results showed that compared with ApoE$^{-/-}$Irgm1$^{+/+}$ mice, the proportion of collagen content in ApoE$^{-/-}$Irgm1$^{+/-}$ mice was significantly increased (Figure 2I, 2L, Supplemental Figure 3F). Cholesterol crystals in the aortic sinus plaque were further examined by laser reflection microscopy, and ApoE$^{-/-}$Irgm1$^{+/+}$ mice showed significantly fewer cholesterol crystals (Figure 2M–N). These results suggest that Irgm1 aggravates the vulnerable phenotype of atherosclerotic plaque *in vivo*.

Irgm1 induces apoptosis in macrophages. Previous studies have demonstrated that autophagy affects progression of atherosclerosis (26, 27). We first observed the relationship between Irgm1 and macrophage autophagy *in vitro* (Supplemental Figure 1). After stimulating the RAW264.7 cells with ox-LDL for 3 h, the fluorescence signals of autophagosomes and lysosomes combined successfully (Supplemental Figure 1D–E). Unfortunately, a 48-h treatment with ox-LDL blocked the autophagic flux (Supplemental Figure 1F–G). Excessive apoptosis of macrophages is a feature of vulnerable plaques (22). We investigated whether Irgm1 promotes macrophage apoptosis during the progression of atherosclerosis. Compared with ApoE$^{-/-}$Irgm1$^{+/+}$ mice, the proportion of TUNEL-positive cells in ApoE$^{-/-}$Irgm1$^{+/-}$ mice was significantly decreased (Figure 3A–B). Expression of cleaved-caspase3 and cleaved-caspase9 in the plaque of ApoE$^{-/-}$Irgm1$^{+/-}$ mice was also significantly decreased (Figure 3C–E). These results indicate that Irgm1 can induce apoptosis in plaques. Next ,we assessed whether Irgm1 induces macrophage apoptosis *in vitro*. The qPCR showed that si-Irgm1 knocked down Irgm1 expression effectively (Supplemental Figure 1A). To strengthen our conclusion, we analyzed the effect of si-Irgm1 on the activities of cleaved-caspase3/9. Compared with the si-control group, cleavage caspase3 and cleavage caspase9 activities of the si-Irgm1 group were reduced (Figure 3F-G), consistent with western blotting results (Figure 3H-I). Furthermore, compared with ApoE$^{-/-}$Irgm1$^{+/+}$ mice, apoptosis of peritoneal

macrophages in ApoE$^{-/-}$Irgm1$^{+/-}$ mice was reduced (Figure 3G, 3M). Finally, in vivo, we investigated effects of Irgm1 on expression of cleaved-caspase3 and cleaved-caspase9 in macrophages (CD11b). The results showed the co-localization ratio in the ApoE$^{-/-}$Irgm1$^{+/-}$ mice plaques was significantly reduced (Figure 3K–L, Figure 3N–O). In summary, these results confirmed that Irgm1 promote macrophage apoptosis both *in vivo* and *in vitro*.

ROS contributes to Irgm1-induced apoptosis in macrophages. Production and accumulation of ROS in macrophages contributes to apoptosis (28). We used DHE fluorescent probes to label ROS production in Raw264.7 cells. Compared with the si-control group, DHE fluorescence intensity of the si-Irgm1 group declined sharply (Figure 4A-4B), consistent with flow cytometry results (Figure 4C-4D). These results indicate that Irgm1 can promote production of intracellular ROS in macrophages. We next assessed whether ROS were involved in *Irgm1*-induced apoptosis. Compared with the si-control group, the expression of cleaved-caspase3 and cleaved-caspase9 were reduced in the si-Irgm1 group. N-acetylcysteine (NAC, an active oxygen scavenger) further reduced expression of cleaved caspase3 and caspase9 (Figure 4E-4F), and the activities of caspase3 and caspase9 showed similar results (Figure 4G–4H). Compared with the si-control group, the co-localized fluorescence intensity of TUNEL and DAPI in the si-Irgm1 group was significantly reduced , which was

further decreased in the presence of NAC (Figure 4I–4J). In summary, Irgm1 induces apoptosis in macrophages by promoting production of ROS.

Irgm1 induces apoptosis in macrophages by activating MAPK signaling pathway. MAPK signaling has been implicated in apoptosis through the JNK/P38/ERK pathway in response to various stress stimuli, including ROS (29). To explore how Irgm1 leads to macrophage apoptosis, we detected phosphorylated (p)-JNK, p-p38, and p-ERK in the MAPK signaling pathways, as well as the downstream apoptosis-related proteins Bax, Bcl2, cleaved-caspase3, and cleaved-caspase9. Compared with the si-control group, expression of p-JNK, p-p38, p-ERK, Bax, cleaved-caspase3, and cleaved-caspase9 were significantly decreased in the si-Irgm1 group. Bcl2 expression was increased (Figure 5A Lane 1,2 vs. Lane 3,4; Figure 5B–5C). NAC further decreased expression of p-JNK, p-p38, p-ERK, and downstream apoptotic proteins Bax, cleaved-caspase3, and cleaved-caspase9 in the si-Irgm1 group , and increased expression of Bcl2 (Figure 5A Lane 5,6; Figure 5B–5C). These results suggest that activation of the MAPK signaling pathway and ROS generation were major characteristics of Irgm1-induced apoptosis. To test this conclusion, the macrophages were treated with three inhibitors, including SP600125 (SP), SB203580 (SB) and U0126 (U), which inhibit JNK, P38, and ERK, respectively. Expression of JNK, P38, and ERK was significantly reduced by these inhibitors (Supplementary Figure 4A–F). In both si-control and si-Irgm1 groups, ox-LDL

significantly increased expression of Bax, cleaved-caspase3, and cleaved-caspase9, and decreased expression of Bcl2 (Figure 5D Lane 1 vs. 2; Lane 6 vs. 7; Figure 5E–H). Importantly , these inhibitors prevented the changes of MAPK signaling pathway and apoptosis-related proteins (Figure 5D, lane 3–5 vs. lane 2; Lane 8–10 vs. lane 7; Figure 5H). Together, these results show that Irgm1 induces ROS production, which activates the MAPK signaling pathways, leading to apoptosis in macrophages.

Irgm1 aggravates vulnerability of plaque and macrophage apoptosis in bone marrow chimera mice. We constructed chimera mice to investigate whether Irgm1 expressed on hematopoietic origin cells contributes to atherosclerosis progression. Bone marrow macrophages from ApoE$^{-/-}$Irgm1$^{+/+}$ or ApoE$^{-/-}$Irgm1$^{+/-}$ mice were transferred to ApoE$^{-/-}$Irgm1$^{+/-}$ mice (Figure 6A). Compared with ApoE$^{-/-}$Irgm1$^{+/+}$ mice, cholesterol crystals, thickness of fibrous cap, necrotic core area, ratio, and plaque area were significantly reduced in plaques of ApoE$^{-/-}$Irgm1$^{+/-}$ mice (Figure 6B–6E, 6H, Supplemental Figure 5A). ORO staining showed that the ratio of neutral lipids in ApoE$^{-/-}$Irgm1$^{+/-}$ mice plaques was reduced (Figure 6F, 6I). Compared with ApoE$^{-/-}$Irgm1$^{+/+}$ mice, both content and ratio of collagen fibers in plaques of ApoE$^{-/-}$Irgm1$^{+/-}$ mice were significantly reduced (Figure 6G, 6J; Supplemental Figure 5C). These results were consistent with those in non-recipient mice (Figure 3).

To further test the contribution of Irgm1-induced apoptosis in chimera mice

macrophages, we examined expression of cleaved-caspase3 and cleaved-caspase9 in the aortic sinus. Compared with ApoE$^{-/-}$Irgm1$^{+/+}$ mice, the ratio of cleaved-caspase3 and cleaved-caspase9 in plaques of ApoE$^{-/-}$Irgm1$^{+/-}$ mice was significantly reduced (Figure 6K–6N), consistent with western blotting results (Figure 6O–6Q). Finally, we observed co-localization of cleaved-caspase3 and cleaved-caspase9 with CD68 (Supplemental Figure 5D–5E). In summary, Irgm1 aggravates vulnerability of plaque and contributes to apoptosis in macrophages in chimera mice.

Discussion

In the STEMI cohort, serum IRGM levels were increased in patients with culprit PR (Figure 1B). This potentially provides a tool to predict PR. When adjusted for other risk factors related to ACS, IRGM was still correlated with PR (Figure 1C). Apparently, IRGM/Irgm1 affects the vulnerability of atherosclerotic plaques. In this study, we clarified how Irgm1 affects plaque phenotype *in vivo* and *in vitro*. Irgm1 activates the MAPK signaling pathway by promoting ROS production, leading to macrophage apoptosis and, thus, affecting plaque stability (Figure 7). These data identify a crucial role for Irgm1 in mediating apoptosis of macrophages during the progression of atherosclerosis, and highlight IRGM as a potential predictor of atherosclerotic plaque vulnerability.

In the 1980s, Davies *et al*. showed that PR caused most fatal myocardial infarctions (32). It became accepted that instability of coronary atherosclerosis is due to weakening of the collagen structure caused by inflammatory infiltration and fissure of TCFA plaques (33-34). The emergence of OCT makes it possible to track the pathogenesis of ACS in patients *in vivo* and assess the morphological features of vulnerable plaques (35). Our previous studies found that most of the plaques that tend to rupture have thin fibrous caps and large lipid arcs, as assessed by OCT combined

with intravascular ultrasound (7). Here, we compared the morphological characteristics between ruptured and non-ruptured culprit plaques in patients with STEMI. We confirmed that the fibrous cap of the ruptured plaque was thinner and contained more lipids (Figure 1A). However, there is no good method for the early diagnosis and treatment of PR, mandating a search for biological predictors of PR in ACS patients.

Inflammation plays essential roles in the progression from vulnerable to ruptured plaque, ultimately leading to clinical events (36). Administration of IL-1β monoclonal antibody provided a 15% reduction in the risk of further MI, stroke, or death, proving the effectiveness of anti-inflammatory treatment on atherosclerotic diseases (37). Hunn *et al*. have shown that IRGM belongs to the family of interferon-induced GTPases (IRGs), genetically and functionally related to proteins implicated in chronic inflammatory diseases (38-39). Therefore, we analyzed expression of serum IRGM in patients with STEMI and found that serum IRGM was significantly increased in the RUP group (Figure 1B). Considering TNF-α and IL-6 play central roles in downstream inflammatory responses that lead to atherosclerosis (40), we quantified expression of serum IRGM, IL-6, and TNF-α, and found that expression of IRGM was positively correlated with IL-6 and TNF-α (Supplemental Figure 2D–G). These findings indicate that IRGM/Irgm1 plays a potential role in the progression from

vulnerable to ruptured plaque, ultimately leading to clinical events.

IRGM/Irgm1 has been extensively studied in inflammation and cancer (41, 42). IRGM/Irgm1 promotes macrophage autophagy and protects the intestine from inflammatory attack (39, 43). Human IRGM proteins are targeted by RNA viruses, some of which improve their own replication ability by autophagy (44, 45). Inhibiting the expression of IRGM/Irgm1 by microRNA attenuates autophagy by macrophages (46). Here, we confirmed that IRGM was highly expressed in the RUP group, which was related to the vulnerability of advanced atherosclerotic plaques (Figure 1). We next investigated whether the IRGM/Irgm1-induced macrophage autophagy contributes to vulnerability of atherosclerotic plaques. After a 3-h treatment with ox-LDL, Irgm1 up-regulated mRNA and protein levels of autophagy indicators LC3, P62, Atg5 and beclin1. Treatment with si-Irgm1 increased RFP-positive/GFP-positive puncta, suggesting that si-Irgm1 inhibits autophagosome–lysosome fusion (Supplemental Figure 1). Unfortunately, after stimulating RAW264.7 cells with ox-LDL for 48 h, only RFP-positive/GFP-positive puncta were observed in both the si-Irgm1 and si-control groups. These results suggested that in the early stage of atherosclerosis, Irgm1 may prevent induction of autophagy in macrophages, whereas the autophagy flux of macrophages is blocked in an advanced atherosclerotic model (Supplemental Figure 1). Therefore, the effect of IRGM on macrophage autophagy

cannot explain changes in plaque vulnerability in advanced atherosclerosis.

Evidence has amassed that macrophage apoptosis intensifies formation of plaque necrotic cores, causing thinning of the fibrous cap, and ultimately leading to PR (25, 47) (48-50). In this study, we first explored the effect of Irgm1 on atherosclerotic plaque phenotype in mice. The aortic plaque area, cholesterol crystals, necrotic core, and neutral lipids were reduced in ApoE$^{-/-}$Irgm1$^{+/-}$ mice, whereas collagen fibers increased. These results indicate that Irgm1 can aggravate the vulnerability characteristics of advanced atherosclerotic plaques (Figure 2). Next, we found that Irgm1 promotes expression of apoptosis-related proteins cleaved-caspase3 and cleaved-caspase9 in macrophages (Figure 3), also confirmed *in vitro*. Finally, Irgm1 deficiency in bone marrow *chimera* mice displayed significant delays in atherosclerotic progression and had stabilized plaques (Figure 6). In summary, IRGM/Irgm1 contributes to plaque vulnerability by promoting macrophage apoptosis in advanced atherosclerotic plaques but mechanisms remain unclear. Hypotheses proposed to explain the apoptosis of macrophages in advanced atherosclerosis include deprivation of growth factors or the presence of toxic cytokines (51, 52), yet there is no evidence for these hypotheses *in vivo*.

Many studies have explored the continuous accumulation of ROS, triggering

depolarization of the inner mitochondrial membrane and eventually leading to cell apoptosis (48, 59). Markers of endoplasmic reticulum stress and macrophage apoptosis are found in human atherosclerotic plaques. Here, we detected reactive oxygen fluorescent probes *in vitro* and found that Irgm1 can promote ROS production in macrophages. Interestingly, ROS scavenger NAC and si-Irgm synergistically reduce levels of apoptosis-related proteolytic caspase3 and caspase9 in RAW264.7 cells. These results suggest that Irgm1 can lead to apoptosis *in vitro* by promoting ROS production in macrophages. Increased accumulation of ROS activates MAPK (53-56). Other studies have shown that the MAPK signaling pathway is regulated by ERK1/2, c-Jun N-terminal kinase1/2/3 (JNK1/2/3), and p38-MAPK in the processes of autophagy, apoptosis, and inflammation (61, 62). We speculate that Irgm1 promotes ROS production in macrophages and activates apoptosis via the MAPK signaling pathway. Compared with the control group, when macrophages were treated with ERK1/2, JNK, and p38-MAPK inhibitors, expression of the apoptotic proteins BAX, Bcl-2, *cleaved-caspase*3, and *cleaved-caspase*9 was significantly reduced (Figure 5). In summary, these results indicate that Irgm1 can activate the MAPK signaling pathway and cause macrophage apoptosis.

These results are subject to limitations. First, as a retrospective study, the clinical data reflect the current epidemiological, serum, and plaque features of Chinese patients

with STEMI. It may not be generalizable to patients with NSTE-ACS or patients from other locations. Second, although macrophage infiltration is defined in a published consensus on OCT, it remains a controversial topic to recognize macrophage infiltration by OCT. Therefore, this study did not list the data of macrophage infiltration by OCT between the RUP and NO-RUP groups. Third, as we could not obtain coronary arteries from clinical patients, our research group used lower limb arteries obtained from vascular surgery to assess plaque characteristics. This may not accurately reflect the profile of coronary plaques. Fourth, since ApoE$^{-/-}$Irgm1$^{-/-}$ mice in the C57BL/6 background may be embryonic lethal, we have been unable to obtain the above double-gene knockout mice. Here, we were only able to use ApoE$^{-/-}$Irgm1$^{+/-}$ mice as the experimental group *in vivo*. Fifth, it may be important to study the progression of atherosclerotic plaques by establishing an atherosclerosis model through a high-fat diet. However, this modeling method may not be representative for the study of PR. We are actively seeking a way to construct a PR model to compensate for drawbacks of this research. Based on our conclusions, we have abundant reasons to regard Irgm1 as a suitable predictive factor for rupture in the rupture model of advanced atherosclerotic mice. Sixth, we found that Irgm1 regulates macrophage apoptosis by activating the MAPK signaling pathway. Others and we have not yet verified the specific site at which Irgm1 acts in regulating the MAPK signaling pathway. Seventh, in the sequence of IRGM (+313) (rs10065372), an SNP is present at position +313 inside exon 2 of IRGM at chromosome 5q33.1. This SNP is

associated with severe sepsis with a high fatality rate. It is not clear whether mouse Irgm1 has the same SNP as human IRGM. We must keep in mind these limitations, but our findings reinforce each other due to the multiplicity of approaches.

Methods

Study Participants. In this study, 135 patients who were diagnosed with STEMI in the 2nd Affiliated Hospital of Harbin Medical University (Harbin, China) between August and December 2016 and who underwent OCT after thrombus aspiration were enrolled. Main exclusion criteria were angina pectoris, myocarditis, heart failure, aortic dissection, acute and chronic infections and infectious diseases, liver and kidney insufficiency, and severe progressive diseases. We finally enrolled 85 patients with STEMI. We divided patients into two groups: patients with PR (RUP group) (n = 52) and without PR (NO-RUP group) (n = 33). Eight additional healthy volunteers were also recruited. We analyzed OCT images and obtained the serum of these 85 patients and 8 healthy volunteers. The definition of STEMI was in accordance with the 2015 ACC/AHA/SCAI guidelines published previously (63).

OCT Image Acquisition and analysis. The frequency-domain OCT ILUMIEN system, along with the Dragon fly catheter (St. Jude Medical, Westford, Massachusetts, USA) were used to acquire OCT imaging of culprit lesions, as shown previously (9). Two experienced independent investigators (H.C and S.S) analyzed OCT images according to the criteria of the Consensus OCT Document (64) using a proprietary OCT review workstation (St. Jude Medical, Westford, MA, USA) at an intravascular imaging and

physiology core lab. If these two observers disagreed, a consensus reading was obtained by judgement with another investigator. Investigators were blinded to the subject information. Plaque rupture was defined as a lipid plaque with fibrous cap continuity destroyed plus a clear cavity formation within the plaque. The FCT covering the lipid core was measured three times at the thinnest location, and the mean value of triplicate measurements was calculated. TCFA was a lipid plaque in the presence of FCT < 65 μm with a maximum lipid arc of at least 90° (65).

Patient blood vessel specimens. Atherosclerotic middle artery vessels were obtained from patients with arterial occlusion in the Department of Vascular Surgery of the First Affiliated Hospital of Harbin Medical University. Normal vessels were obtained from five patients who underwent lower limb amputation. Blood vessel specimens from patients were transported to the laboratory by dry ice and maintained at low temperature (−40 °C) after isolation. Blood vessel specimens were embedded in paraffin and sectioned consecutively (4 μm) for H&E and immunohistochemical staining.

Animals. Irgm1$^{-/-}$ mice (C57BL/6 background) were derived from a published source (17). Irgm1$^{-/-}$ mice and ApoE$^{-/-}$ mice were crossed to obtain ApoE$^{+/-}$Irgm1$^{+/-}$ mice. We screened ApoE$^{-/-}$Irgm1$^{+/-}$ mice by crossing ApoE$^{+/-}$Irgm1$^{+/-}$ mice. Due to the

probability of embryonic lethality in ApoE$^{-/-}$Irgm1$^{-/-}$ mice, we genetically identified offspring of self-crossed ApoE$^{-/-}$Irgm1$^{+/-}$ mice. After PCR genotyping, we then established a model of advanced atherosclerosis in mice fed high-fat diet for sixteen weeks.

Reagents. See Supplemental Table 3–4.

Bone marrow chimera recipient mice. ApoE$^{-/-}$Irgm1$^{+/+}$ (6–8 weeks old) recipient mice were supplemented with fradiomycin, polymyxin, and sterile pH 3.0 water for a week. They were then irradiated with 9 Gy of radiation.

The recipient mice were divided into three groups. Two groups of recipient mice received bone marrow macrophages (5**Error! Reference source not found.**10^6) from ApoE$^{-/-}$Irgm1$^{+/+}$ donor mice and ApoE$^{-/-}$Irgm1$^{+/-}$ donor mice by tail vein injection, whereas the control group received saline. After about seven days, the control group died and the experimental group survived, indicating that the modeling was successful.

Cell culture. Raw264.7 cells were cultured in Dulbecco's Modified Eagle's medium (DMEM) (SH30022.01B, HYCLONE, USA) containing 10% FBS (0500, ScienCell,

USA). Cells were seeded in 60 mm dishes or 6- and 12-well plates and collected at 60%–80% confluency.

Transfection. Transfection was accomplished using Lipo3000 (L3000008, Invitrogen, USA) according to manufacturer's protocols with the following siRNA duplexes: negative control, 5'-CGUACGCGGAAUACUUCGAUU-3'; Irgm1-siRNA, 5'-GGGCUGGGAUUCUGUCAUA-3'. Real-time qPCR was utilized to confirm efficiency of transfection.

ROS detection. ROS generated by ox-LDL treatment in cells was evaluated by fluorescence intensity of the dihydroethidium (DHE) probe. After the intake of ox-LDL, macrophages were harvested, washed, and incubated with 5 μM DHE probe (S0063, Beyotime, China) for 30 min at 37 °C in the dark. After rinsing, fluorescent signals were immediately measured using a fluorescence microscope and FACS Verse flow cytometer (BD, USA).

Real-time quantitative PCR (RT-qPCR). Total RNA extracted by TRIzol reagent (Thermo Fisher, USA) was reverse-transcribed utilizing the RT Easy II First Strand cDNA Synthesis Kit (04379012001, Roche, Switzerland). We amplified cDNA (18 ng)

in a Real-Time PCR Easy (SYBR Green I) (HY-K0501, MCE, China) on Bio-RAD Sequence Detection system (Bio-RAD, USA). The following primers were used in Supplemental Table 5, Gene expression values were normalized against β-actin.

Pathological staining. We placed hearts in a mold containing tissue-freezing medium, which was perfused with PBS and frozen. Eight μm-thick (H&E staining) and twenty μm-thick (ORO staining) sections were cut from the hearts, from caudal of the aortic sinus to the proximal aorta. Slides were fixed with 4% paraformaldehyde and then stained. H&E, ORO, and Masson staining are as previously described (17).

Immunofluorescence. Frozen slides were rewarmed at RT for 10 min, and then fixed with cold acetone (−20 °C) for 10 min. After rinsing three times in distilled water, slides were incubated with 0.3% Triton-X 100 for 30 min at 37 °C, and incubated with primary antibody at 4 °C overnight. On day 2, after rewarming for 10 min at room temperature (RT), slides were incubated with secondary antibody at RT for 1 h. Finally, nuclei were stained with 0.5 g/L DAPI for 10 min and images were captured using a confocal laser scanning microscope (ZEISS LSM 700).

Immunohistochemistry. Frozen slides were rewarmed at RT for 10 min, and then fixed

with cold acetone (−20 °C) for another 10 min. After three rinses in distilled water, slides were incubated with 0.3% Triton-X 100 for 30 min at 37 °C. Endogenous peroxidase was blocked with 3% hydrogen peroxide, and slides were incubated with primary antibody at 4 °C overnight. On the next day, frozen slides were rewarmed for 10 min at RT and then incubated with secondary antibody at RT for 1 h. Next, slides were exposed to 3,3'-diaminobenzidine (DAB) (ZSGQ-BIO, China) stain for 1–10 min, followed by Hematoxylin stain. Images were taken by ordinary forward microscopy (Olympus, BX41). Paraffin sections were first dewaxed and then fixed with 4% PFA for 5 min. After rinsing with PBS, the sections were incubated with 0.3% Triton-X 100 at 37 °C for 30 min, and then antigen repair proceeded. The rest of the steps were the same as for frozen sections.

Western blotting. Nuclear and cytosolic fractions were obtained using a nuclear/cytosol fractionation kit (R0050, Solarbio, China). Total protein was extracted using RIPA buffer with phenylmethylsulfonyl fluoride, and Halt Protease and Phosphatase Inhibitor. Protein concentration was measured by a bicinchoninic acid protein assay. Protein samples (30 μg) were separated by sodium dodecyl sulfate-polyacrylamide gel electrophoresis (SDS-PAGE, P0015, Beyotime, China) and transferred to 0.22-μm PVDF membranes. After blocking with 5% dried skimmed milk for 2 h at RT in Tris-buffered saline, the membranes were probed with primary antibodies (1:1000) and

incubated overnight at 4 °C. Membranes were incubated for 2 h in the presence of horseradish peroxidase (HRP)-conjugated secondary antibodies (1:8000) at RT. Immunoreactivity was visualized by chemiluminescence using a ChemiDoc™ MP Imaging System (Tanon, China). Protein bands were quantified using a Bio-Rad Chemi EQ densitometer and Bio-Rad Quantity One software (Tanon, China) and normalized to GAPDH.

Caspase-3/9 Activity. Caspase‑3/9 activity in the vascular tissue or cell homogenates was evaluated using the Caspase‑3 Assay Kit or Caspase‑9 Assay kit according to manufacturer's instructions.

Genotyping. Excised mouse toes were added to 100 μL tissue digestion solution (bimake) and digested for 15 min at 55 °C, then incubated for 5 min at 95 °C to inactivate enzymes. Tubes were centrifuged at 12,000 rpm for 5 min, with supernatant used as the PCR template (1000 ng). Primer sequences are listed in supplementary table 6. Next, PCR amplification was performed, followed by agarose gel electrophoresis and imaging analysis using a gel imaging system (BIO RAD, GelDoc Go).

Autophagy with double-labeled adenovirus. Raw264.7 cells were transfected with si-Irgm1 for 24 h. Adenovirus vectors encoding LC3 (HBAD-mRFP-GFP-LC3, HANBIO, China) and ox-LDL (50 μg/mL) were added for 3 h or 48 h. Transfection efficiency was detected by confocal laser scanning microscope (ZEISS LSM 700). Autophagosomes were represented by the co-localized yellow fluorescence of both GFP and RFP. Due to quenching of GFP signal in acidic compartments, it shows stronger red fluorescence and less co-localization in autolysosomes. LC3 activation was represented by punctate dots in GFP-LC3 transfected cells.

Detection of apoptotic cells by flow cytometry. Cells were cultured and incubated in a 5% CO2 atmosphere for 48 h at 37 °C and then harvested, washed twice with pre-chilled PBS, and resuspended in 200 μL of 1× binding buffer. The cells were stained with fluorescein isothiocyanate (FITC)-conjugated annexin V and propidium iodide (PI) using the Annexin V-FITC & PI Apoptosis Detection Kit (货号, BD Biosciences, USA).

Statistics. Statistical analyses were performed using SPSS version 20.0 (SPSS, Inc., Chicago, IL, USA) or GraphPad Prism 7.0 (GraphPad Software). Continuous variables were expressed as mean ± SD for normally distributed variables and as median (25, 75th percentiles) for non-normally distributed variables, and assessed by

Student *t-test* or Mann-Whitney U test, respectively. Categorical variables were presented as counts and percentages, and the comparisons were performed using a Chi-square test or Fisher's exact-test. A series of multiple logistic regression models were used to assess the relationship between the risk of plaque rupture and plasma IRGM levels. A 2-sided p value < 0.05 was considered statistically significant. All data were analyzed by an independent statistician.

Study approval. This study was approved by the Ethics Committee of the 2nd Affiliated Hospital of Harbin Medical University (Harbin, China), and all patients provided written informed consent. Animals were sacrificed by cervical dislocation. Animal experiments were performed according to guidelines approved by the Institutional Animal Care Committee and in compliance with the guidelines from Directive 2010/63/EU of the European Parliament with approval from the Harbin Medical University Ethics Review Board.

Author contributions

SHF, SS, HXC, BS, and BY designed experiments. HXC and SS wrote the draft of the manuscript, followed by editing by SHF, YB, and JWT. SS, XRH, XYZ, JTT, ZYL, and ZZH performed the animal experiments; SHF, HXC, XW, SS, CCL, and WH performed experiments *in vitro*. ZMZ and CCL collected clinical data. HXC, SS, and JWT measured clinical images. SJW and HXC analyzed and visualized clinical results. BS and LMY provided crucial reagents. BY, BS, and JWT take responsibility for accuracy of the analysis of the whole experiment.

Acknowledgments

Dr. Yu was supported by National Key R&D Program (No. 2016YFC1301100, 2016YFC1301101) and Major Instrument Development Project of the National Natural Science Foundation of China (No. 81827806). Dr. Fang was supported by National Natural Science Foundation of China (No. 81870353) and Natural Science Foundation of Heilongjiang Province (No. LH2020H048). The authors thank all participants and staff from the coronary interventional therapy team and the intravascular imaging core laboratory from the 2nd Affiliated Hospital of Harbin Medical University.

References

1. Libby P, and Hansson GK. Inflammation and immunity in diseases of the arterial tree: players and layers. Circ Res. 2015;116(2):307-11.
2. Libby P. Current concepts of the pathogenesis of the acute coronary syndromes. Circulation. 2001;104(3):365-72.
3. Virmani R, Kolodgie FD, Burke AP, Farb A, and Schwartz SM. Lessons from sudden coronary death: a comprehensive morphological classification scheme for atherosclerotic lesions. Arterioscler Thromb Vasc Biol. 2000;20(5):1262-75.
4. Naghavi M, Libby P, Falk E, Casscells SW, Litovsky S, Rumberger J, et al. From vulnerable plaque to vulnerable patient: a call for new definitions and risk assessment strategies: Part I. Circulation. 2003;108(14):1664-72.
5. Higuma T, Soeda T, Abe N, Yamada M, Yokoyama H, Shibutani S, et al. A Combined Optical Coherence Tomography and Intravascular Ultrasound Study on Plaque Rupture, Plaque Erosion, and Calcified Nodule in Patients With ST-Segment Elevation Myocardial Infarction: Incidence, Morphologic Characteristics, and Outcomes After Percutaneous Coronary Intervention. JACC Cardiovasc Interv. 2015;8(9):1166-76.
6. Jia H, Abtahian F, Aguirre AD, Lee S, Chia S, Lowe H, et al. In vivo diagnosis of plaque erosion and calcified nodule in patients with acute coronary

syndrome by intravascular optical coherence tomography. J Am Coll Cardiol. 2013;62(19):1748-58.

7. Tian J, Ren X, Vergallo R, Xing L, Yu H, Jia H, et al. Distinct morphological features of ruptured culprit plaque for acute coronary events compared to those with silent rupture and thin-cap fibroatheroma: a combined optical coherence tomography and intravascular ultrasound study. J Am Coll Cardiol. 2014;63(21):2209-16.

8. Burke AP, Farb A, Malcom GT, Liang YH, Smialek J, and Virmani R. Coronary risk factors and plaque morphology in men with coronary disease who died suddenly. N Engl J Med. 1997;336(18):1276-82.

9. Dai J, Xing L, Jia H, Zhu Y, Zhang S, Hu S, et al. In vivo predictors of plaque erosion in patients with ST-segment elevation myocardial infarction: a clinical, angiographical, and intravascular optical coherence tomography study. Eur Heart J. 2018;39(22):2077-85.

10. Kang SJ, Mintz GS, Weisz G, Mehran R, Rabbani LE, Verheye S, et al. Age-related effects of smoking on coronary artery disease assessed by gray scale and virtual histology intravascular ultrasound. Am J Cardiol. 2015;115(8):1056-62.

11. Dai J, Xing L, Hou J, Jia H, Hu S, Tian J, et al. Chronic kidney disease predicts coronary plaque vulnerability: an optical coherence tomography study. Coron Artery Dis. 2017;28(2):135-44.

12. MacMicking JD, Taylor GA, and McKinney JD. Immune control of tuberculosis by IFN-gamma-inducible LRG-47. Science. 2003;302(5645):654-9.

13. Hunn JP, Koenen-Waisman S, Papic N, Schroeder N, Pawlowski N, Lange R, et al. Regulatory interactions between IRG resistance GTPases in the cellular response to Toxoplasma gondii. EMBO J. 2008;27(19):2495-509.

14. Rogala AR, Schoenborn AA, Fee BE, Cantillana VA, Joyce MJ, Gharaibeh RZ, et al. Environmental factors regulate Paneth cell phenotype and host susceptibility to intestinal inflammation in Irgm1-deficient mice. Dis Model Mech. 2018;11(2).

15. Tian L, Li L, Xing W, Li R, Pei C, Dong X, et al. IRGM1 enhances B16 melanoma cell metastasis through PI3K-Rac1 mediated epithelial mesenchymal transition. Sci Rep. 2015;5:12357.

16. Xia F, Li R, Wang C, Yang S, Tian L, Dong H, et al. IRGM1 regulates oxidized LDL uptake by macrophage via actin-dependent receptor internalization during atherosclerosis. Sci Rep. 2013;3:1867.

17. Fang S, Xu Y, Zhang Y, Tian J, Li J, Li Z, et al. Irgm1 promotes M1 but not M2 macrophage polarization in atherosclerosis pathogenesis and development. Atherosclerosis. 2016;251:282-90.

18. Wang W, Liu W, Fidler T, Wang Y, Tang Y, Woods B, et al. Macrophage Inflammation, Erythrophagocytosis, and Accelerated Atherosclerosis in Jak2

(V617F) Mice. Circ Res. 2018;123(11):e35-e47.

19. Kasikara C, Doran AC, Cai B, and Tabas I. The role of non-resolving inflammation in atherosclerosis. J Clin Invest. 2018;128(7):2713-23.

20. Hasegawa H, Watanabe T, Kato S, Toshima T, Yokoyama M, Aida Y, et al. The role of macrophage transcription factor MafB in atherosclerotic plaque stability. Atherosclerosis. 2016;250:133-43.

21. Colin S, Chinetti-Gbaguidi G, and Staels B. Macrophage phenotypes in atherosclerosis. Immunol Rev. 2014;262(1):153-66.

22. Sun W, Lin Y, Chen L, Ma R, Cao J, Yao J, et al. Legumain suppresses OxLDL-induced macrophage apoptosis through enhancement of the autophagy pathway. Gene. 2018;652:16-24.

23. Tajbakhsh A, Kovanen PT, Rezaee M, Banach M, Moallem SA, and Sahebkar A. Regulation of efferocytosis by caspase-dependent apoptotic cell death in atherosclerosis. Int J Biochem Cell Biol. 2020;120:105684.

24. Wu Y, Zhang Y, Dai L, Wang Q, Xue L, Su Z, et al. An apoptotic body-biomimic liposome in situ upregulates anti-inflammatory macrophages for stabilization of atherosclerotic plaques. J Control Release. 2019;316:236-49.

25. Wang D, Wang W, Lin W, Yang W, Zhang P, Chen M, et al. Apoptotic cell induction of miR-10b in macrophages contributes to advanced atherosclerosis progression in ApoE-/- mice. Cardiovasc Res. 2018;114(13):1794-805.

26. Fleiner M, Kummer M, Mirlacher M, Sauter G, Cathomas G, Krapf R, et al. Arterial neovascularization and inflammation in vulnerable patients: early and late signs of symptomatic atherosclerosis. Circulation. 2004;110(18):2843-50.

27. Tabas I. Macrophage death and defective inflammation resolution in atherosclerosis. Nat Rev Immunol. 2010;10(1):36-46.

28. Assolini JP, Tomiotto-Pellissier F, da Silva Bortoleti BT, Goncalves MD, Sahd CS, Carloto ACM, et al. Diethyldithiocarbamate encapsulation reduces toxicity and promotes leishmanicidal effect through apoptosis-like mechanism in promastigote and ROS production by macrophage. J Drug Target. 2020;28(10):1110-23.

29. Mi Y, Xiao C, Du Q, Wu W, Qi G, and Liu X. Momordin Ic couples apoptosis with autophagy in human hepatoblastoma cancer cells by reactive oxygen species (ROS)-mediated PI3K/Akt and MAPK signaling pathways. Free Radic Biol Med. 2016;90:230-42.

32. Davies MJ, and Thomas A. Thrombosis and acute coronary-artery lesions in sudden cardiac ischemic death. N Engl J Med. 1984;310(18):1137-40.

33. Falk E, Shah PK, and Fuster V. Coronary plaque disruption. Circulation. 1995;92(3):657-71.

34. Finn AV, Nakano M, Narula J, Kolodgie FD, and Virmani R. Concept of vulnerable/unstable plaque. Arterioscler Thromb Vasc Biol.

2010;30(7):1282-92.

35. Tearney GJ. Intravascular optical coherence tomography. Eur Heart J. 2018;39(41):3685-6.

36. Libby P. Molecular bases of the acute coronary syndromes. Circulation. 1995;91(11):2844-50.

37. Ridker PM, Everett BM, Thuren T, MacFadyen JG, Chang WH, Ballantyne C, et al. Antiinflammatory Therapy with Canakinumab for Atherosclerotic Disease. N Engl J Med. 2017;377(12):1119-31.

38. Hunn JP, Feng CG, Sher A, and Howard JC. The immunity-related GTPases in mammals: a fast-evolving cell-autonomous resistance system against intracellular pathogens. Mamm Genome. 2011;22(1-2):43-54.

39. Mehto S, Jena KK, Nath P, Chauhan S, Kolapalli SP, Das SK, et al. The Crohn's Disease Risk Factor IRGM Limits NLRP3 Inflammasome Activation by Impeding Its Assembly and by Mediating Its Selective Autophagy. Mol Cell. 2019;73(3):429-45 e7.

40. Haddy N, Sass C, Droesch S, Zaiou M, Siest G, Ponthieux A, et al. IL-6, TNF-alpha and atherosclerosis risk indicators in a healthy family population: the STANISLAS cohort. Atherosclerosis. 2003;170(2):277-83.

41. Amersfoort J, Douna H, Schaftenaar FH, Foks AC, Kroner MJ, van Santbrink PJ, et al. Defective Autophagy in T Cells Impairs the Development of Diet-Induced Hepatic Steatosis and Atherosclerosis. Front Immunol.

2018;9:2937.

42. Liu F, Xue H, Ke J, Wu Y, Yao K, Liang S, et al. Ipr1 Regulation by Cyclic GMP-AMP Synthase/Interferon Regulatory Factor 3 and Modulation of Irgm1 Expression via p53. Mol Cell Biol. 2020;40(8).

43. Mehto S, Chauhan S, Jena KK, Chauhan NR, Nath P, Sahu R, et al. IRGM restrains NLRP3 inflammasome activation by mediating its SQSTM1/p62-dependent selective autophagy. Autophagy. 2019;15(9):1645-7.

44. Gregoire IP, Richetta C, Meyniel-Schicklin L, Borel S, Pradezynski F, Diaz O, et al. IRGM is a common target of RNA viruses that subvert the autophagy network. PLoS Pathog. 2011;7(12):e1002422.

45. Gregoire IP, Rabourdin-Combe C, and Faure M. Autophagy and RNA virus interactomes reveal IRGM as a common target. Autophagy. 2012;8(7):1136-7.

46. Yang B, Xue Q, Guo J, Wang X, Zhang Y, Guo K, et al. Autophagy induction by the pathogen receptor NECTIN4 and sustained autophagy contribute to peste des petits ruminants virus infectivity. Autophagy. 2020;16(5):842-61.

47. Cong G, Yan R, Huang H, Wang K, Yan N, Jin P, et al. Involvement of histone methylation in macrophage apoptosis and unstable plaque formation in methionine-induced hyperhomocysteinemic ApoE(-/-) mice. Life Sci. 2017;173:135-44.

48. Xiao Q, Che X, Cai B, Tao Z, Zhang H, Shao Q, et al. Macrophage autophagy regulates mitochondria-mediated apoptosis and inhibits necrotic core

formation in vulnerable plaques. J Cell Mol Med. 2020;24(1):260-75.

49. Yang J, Lin X, Wang L, Sun T, Zhao Q, Ma Q, et al. LncRNA MALAT1 Enhances ox-LDL-Induced Autophagy through the SIRT1/MAPK/NF-kappaB Pathway in Macrophages. Curr Vasc Pharmacol. 2020;18(6):652-62.

50. Wang ZH, Shang YY, Zhang S, Zhong M, Wang XP, Deng JT, et al. Silence of TRIB3 suppresses atherosclerosis and stabilizes plaques in diabetic ApoE-/-/LDL receptor-/- mice. Diabetes. 2012;61(2):463-73.

51. Rusetskaya NY, Fedotov IV, Koftina VA, and Borodulin VB. [Selenium compounds in redox regulation of inflammation and apoptosis]. Biomed Khim. 2019;65(3):165-79.

52. Chen JH, Riazy M, Smith EM, Proud CG, Steinbrecher UP, and Duronio V. Oxidized LDL-mediated macrophage survival involves elongation factor-2 kinase. Arterioscler Thromb Vasc Biol. 2009;29(1):92-8.

53. Su X, Shen Z, Yang Q, Sui F, Pu J, Ma J, et al. Vitamin C kills thyroid cancer cells through ROS-dependent inhibition of MAPK/ERK and PI3K/AKT pathways via distinct mechanisms. Theranostics. 2019;9(15):4461-73.

54. Fan J, Ren D, Wang J, Liu X, Zhang H, Wu M, et al. Bruceine D induces lung cancer cell apoptosis and autophagy via the ROS/MAPK signaling pathway in vitro and in vivo. Cell Death Dis. 2020;11(2):126.

55. Gonzalez L, Qian AS, Tahir U, Yu P, and Trigatti BL. Sphingosine-1-Phosphate Receptor 1, Expressed in Myeloid Cells, Slows

Diet-Induced Atherosclerosis and Protects against Macrophage Apoptosis in Ldlr KO Mice. Int J Mol Sci. 2017;18(12).

56. Cominacini L, Garbin U, Mozzini C, Stranieri C, Pasini A, Solani E, et al. The atherosclerotic plaque vulnerability: focus on the oxidative and endoplasmic reticulum stress in orchestrating the macrophage apoptosis in the formation of the necrotic core. Curr Med Chem. 2015;22(13):1565-72.

57. Signorelli S, Tarkowski LP, Van den Ende W, and Bassham DC. Linking Autophagy to Abiotic and Biotic Stress Responses. Trends Plant Sci. 2019;24(5):413-30.

58. Guo QQ, Wang SS, Zhang SS, Xu HD, Li XM, Guan Y, et al. ATM-CHK2-Beclin 1 axis promotes autophagy to maintain ROS homeostasis under oxidative stress. EMBO J. 2020;39(10):e103111.

59. Singh N, Lawana V, Luo J, Phong P, Abdalla A, Palanisamy B, et al. Organophosphate pesticide chlorpyrifos impairs STAT1 signaling to induce dopaminergic neurotoxicity: Implications for mitochondria mediated oxidative stress signaling events. Neurobiol Dis. 2018;117:82-113.

60. Zhang G, He J, Ye X, Zhu J, Hu X, Shen M, et al. beta-Thujaplicin induces autophagic cell death, apoptosis, and cell cycle arrest through ROS-mediated Akt and p38/ERK MAPK signaling in human hepatocellular carcinoma. Cell Death Dis. 2019;10(4):255.

61. Hammouda MB, Ford AE, Liu Y, and Zhang JY. The JNK Signaling Pathway

in Inflammatory Skin Disorders and Cancer. Cells. 2020;9(4).

62. Silva SLR, Baliza IRS, Dias RB, Sales CBS, Rocha CAG, Soares MBP, et al. Ru(II)-thymine complex causes DNA damage and apoptotic cell death in human colon carcinoma HCT116 cells mediated by JNK/p38/ERK1/2 via a p53-independent signaling. Sci Rep. 2019;9(1):11094.

63. Levine GN, Bates ER, Blankenship JC, Bailey SR, Bittl JA, Cercek B, et al. 2015 ACC/AHA/SCAI Focused Update on Primary Percutaneous Coronary Intervention for Patients With ST-Elevation Myocardial Infarction: An Update of the 2011 ACCF/AHA/SCAI Guideline for Percutaneous Coronary Intervention and the 2013 ACCF/AHA Guideline for the Management of ST-Elevation Myocardial Infarction. J Am Coll Cardiol. 2016;67(10):1235-50.

64. Tearney GJ, Regar E, Akasaka T, Adriaenssens T, Barlis P, Bezerra HG, et al. Consensus standards for acquisition, measurement, and reporting of intravascular optical coherence tomography studies: a report from the International Working Group for Intravascular Optical Coherence Tomography Standardization and Validation. J Am Coll Cardiol. 2012;59(12):1058-72.

65. Prati F, Regar E, Mintz GS, Arbustini E, Di Mario C, Jang IK, et al. Expert review document on methodology, terminology, and clinical applications of optical coherence tomography: physical principles, methodology of image acquisition, and clinical application for assessment of coronary arteries and atherosclerosis. Eur Heart J. 2010;31(4):401-15.

Figure legends

Figure 1. IRGM is associated with atherosclerotic plaque rupture in patients with STEMI, and highly expressed in patients with atherosclerotic plaque. (A) Representative OCT images in normal coronary vessels, NO-RUP plaques and RUP plaques; arrows show TCFA, with FCT < 65 μm, as well as lipid arc > 90°; asterisks represent ruptured cavities at the culprit site. (B) Serum IRGM levels among healthy volunteers, NO-RUP patients and RUP patients. *$p < 0.05$; ##$p < 0.01$; &$p < 0.05$. (C) Adjusted ORs and 95% CIs for plaque rupture associated with serum IRGM in patients with STEMI by 4 models: Model 1, adjusted for age; Model 2, in which Model 1 was further adjusted for hypertension, diabetes mellitus and current smoking; Model 3, in which Model 2 was additionally adjusted for lipid factors (LDL-C and TC) and Model 4, in which Model 3 was further adjusted for peak TnI and hs-CRP. (D) Representative images of the detection of the expression of IRGM and CD68 in atherosclerotic plaques and normal vessels of the human lower limbs. H&E staining is also shown. Scale bars = 100 μm. (E, F) Quantification of the percentage of $IRGM^+$ and $CD68^+$ areas in intimal plaques. *$p < 0.05$; ns = no significance.

Figure 2. Irgm1 can affect atherosclerotic lesion phenotype in vivo. (A) Genotype analyses for IRGM; Lane 1, 2, 4, 6, 7 and 9 represent ApoE$^{-/-}$Irgm1$^{+/+}$ mice, Lane 3, 5, 8 and 10 represent ApoE$^{-/-}$Irgm1$^{+/-}$ mice. (B) Study design for establishment of advancing atherosclerotic plaques in mice. After being given a high-fat diet for 16 weeks, mice were sacrificed and frozen or paraffin slices of tissues prepared for staining. HFD = high-fat diet; wks = weeks. (C, D) Representative images and quantitative analyses of ORO staining in three parts of the aorta: aortic arch (AA) (n = 4), thoracic aorta (TA) (n = 4), and abdominal aorta (Ad.A) (n = 4). (E) Representative images for H&E staining to assess the FCT, necrotic lipid core and plaque areas in the aortic sinus (n = 10). Necrotic lipid cores are denoted by *; black dashed lines indicate the contour of the plaques; scale bars = 200 μm. (F, G) Quantitative analyses of plaque areas and FCT (n=10). (J) Percentage of necrotic core areas in the plaques (n = 10). (H) Neutral lipid was detected in the aortic sinus by ORO staining (n = 10); scale bars = 200 μm. (I) Representative images for the detection of collagen in the aortic sinus as revealed by Masson staining (n = 10); scale bars = 200 μm. (K, L) Quantitative analyses of the percentage of neutral lipid and collagen content in the plaques, respectively. (M) Representative images of cholesterol crystals observed by confocal microscopy (n = 8~9); scale bars = 50 and 100 μm. (N) Quantitative analyses of the proportion of cholesterol crystals in the plaque. A^{-}I^{+}= ApoE$^{-/-}$Irgm1$^{+/+}$ mice; A^{-}I^{-}= ApoE$^{-/-}$Irgm1$^{+/-}$ mice; *$p < 0.05$, **$p < 0.01$, ***$p < 0.001$; ns=no significance. Results are presented as the mean ± SD. Statistical

analysis: unpaired Student's *t-test*.

Figure 3. Irgm1 induces apoptosis in macrophages. (A) TUNEL^{+} cell areas in aortic sinus plaques from ApoE$^{-/-}$Irgm1$^{+/+}$ (n = 3) and ApoE$^{-/-}$Irgm1$^{+/-}$ mice (n = 3). Areas circled by dashed lines represent the contour of plaques; scale bars = 200 μm. (B) Quantification of the percentage of TUNEL^{+} areas within the plaques. (C-E) Representative images(C) and quantitative analyses (D, E) of cleaved-caspase3 and cleaved-caspase9 in the plaques (n = 3); NC=negative control; scale bars = 100 μm. (F–H) Raw264.7 cells were transfected with si-Irgm1, and then stimulated with ox-LDL (50 ng/ml) for 48 h. Activity of cleaved-caspase3 (F) and cleaved-caspase9 (G) was quantified. (H-I) Western blotting was used to detect the expression of cleaved-caspase3 and cleaved-caspase9(H) and quantitative analyses results were shown (I). Duplicate samples were run in the same gels, with the membrane cut in half. GAPDH was used as a loading control. Quantitative data represent the fold change after normalized to GAPDH. (J-O) ApoE$^{-/-}$Irgm1$^{+/+}$ and ApoE$^{-/-}$Irgm1$^{+/-}$ mice were given a high-fat diet for 16 weeks. (J, M) Peritoneal macrophages were recruited and then FITC-Annexin V and PE-PI were co-stained and quantified by flow cytometry (n = 4 in each group). (K) Representative images for co-location of cleaved-caspase3 (red) and CD11b (green) by immunofluorescence staining (n = 3 in each group). (L) Co-location of cleaved-caspase9 (red) and CD11b (green) by immunofluorescence staining (n = 3 in each group); nuclei stained by DAPI (blue); scale bars = 200 μm. (N, O) Quantitative data of the co-location percentage of CD11b^{+} with cleaved-caspase3 (N) and cleaved-caspase9 (O). A^{-}I^{+}= ApoE$^{-/-}$Irgm1$^{+/+}$

mice; $A^{-}I^{-}$= $ApoE^{-/-}Irgm1^{+/-}$ mice, *$p < 0.05$, **$P < 0.01$. Results are presented as the mean ± SD. Statistical analysis: unpaired Student's *t-test*.

Figure 4. ROS contributes to Irgm1-induced apoptosis in macrophages. (A-D) The Raw264.7 cells were transfected with si-Irgm1 and si-control, and then stimulated with ox-LDL (50 μg/ml) for 48 h. (A) Representative images of the reactive oxygen species labeled with DHE (5 μM) fluorescent probe were observed by confocal microscopy (n = 3 per group); scale bars = 50 μm. (B) Quantitative data in the graph represent relative mean fluorescence intensity (MFI) (n = 3 per group). (C-D). Flow cytometry was used to detect ROS labeled with DHE fluorescent probes (n = 6 per group). (C) Quantitative data represent the percentage of DHE^+ macrophages and representative graphs showing dot plots (D). (E-J) Raw264.7 cells transfected with si-Irgm1 and si-control, in presence or absence of NAC, and then stimulated with ox-LDL (50 μg/ml) for 48 h. (E) Western blotting was used to detect the expression of cleaved-caspase3 and cleaved-caspase9. Duplicate samples were run in the same gels, with the membrane cut in half. GAPDH was used as a loading control. (F) Quantitative data represent the fold change after normalization to GAPDH. (G, H) The protein activity of cleaved-caspase3 and cleaved-caspase9 was detected by ultraviolet spectrophotometry (n = 3 in each group). (I-J) Representative images(I) and quantitative data(J) for $TUNEL^+$ macrophages (green) by immunofluorescence. nuclei were stained by DAPI (blue). DIC channel shown the contour of cells; scale bars = 50 μm; (n = 3 per group). si-control vs. si-Irgm1, $*p < 0.05$, $**p < 0.01$; si-Irgm1 vs. si-Irgm1+NAC, $\#p < 0.05$, $\#\#p < 0.01$. Results are presented as the mean ± SD. Statistical analysis: unpaired Student's *t-test*.

Figure 5. Irgm1 induces apoptosis in macrophages by activating the MAPK signaling pathways. (A-C) The Raw264.7 cells were transfected with si-Irgm1 and si-control, in presence or absence of NAC, and then stimulated with ox-LDL (50 μg/ml) for 48 h. Representative image(A) and quantitative data(B-C) of p-JNK, p-38, p-ERK and apoptosis-related Bax, Bcl2, cleaved-caspase3 and cleaved-caspase9 protein levels. GAPDH was used as a loading control. Quantitative data representing the fold change after normalized to GAPDH. (D) Expression of Bax, Bcl2, cleaved-caspase3 and cleaved-caspase9 were detected by western blotting in si-control (Lane 1–5) and si-Irgm1 (Lane 6–10) groups, after treatment with SP600125 (10 μM), SB203580 (10 μM) or U0126 (10 μM) for 3 h. GAPDH was used as a loading control. (E–H) Quantitative data representing the fold change after normalization to GAPDH. si-control vs. si-Irgm1 in (B, C): *$p < 0.05$, **$p < 0.01$, ***$p < 0.001$, ****$p < 0.0001$; si-Irgm1 vs. si-Irgm1+NAC, #$p < 0.05$, ##$p < 0.01$; si-control vs. si-Irgm1 in (D–H): Lane 1 vs. Lane 2, Lane 6 vs. Lane 7, *$p < 0.05$, **$p < 0.01$, ***$p < 0.001$; Lane 3, 4, 5 vs. Lane 2; Lane 8, 9, 10 vs. Lane 7, &$p < 0.05$, &&$p < 0.01$. Results are presented as the mean ± SD. Statistical analysis: unpaired Student's *t-test*.

Figure 6. Irgm1 aggravates plaque progression in bone marrow chimera recipient mice and contributes to macrophage apoptosis. (A) Schematic diagram for the establishment of the bone marrow chimera recipient mouse model. Representative images (B) and quantitative analyses (C) of cholesterol crystals from ApoE$^{-/-}$Irgm1$^{+/+}$ (n = 3) and ApoE$^{-/-}$Irgm1$^{+/-}$ (n = 3) bone marrow chimera recipient mice; scale bars = 100 μm. (D) Representative images for H&E staining of plaques in the aortic sinus from ApoE$^{-/-}$Irgm1$^{+/+}$ (n = 5) and ApoE$^{-/-}$Irgm1$^{+/-}$ (n = 3) bone marrow chimera recipient mice. A necrotic lipid core is indicated by *; dashed lines indicate the contour of the plaques; scale bars = 200 μm. (E, H) Quantitative analyses of FCT, and percentage of necrotic core areas in the plaques. (F) Representative images of neutral lipid in the aortic sinus detected by ORO staining from ApoE$^{-/-}$Irgm1$^{+/+}$ (n = 5) and ApoE$^{-/-}$Irgm1$^{+/-}$ (n = 3) bone marrow chimera recipient mice; scale bars = 200 μm. (G) Representative images of collagen in the aortic sinus detected by Masson staining from ApoE$^{-/-}$Irgm1$^{+/+}$ (n = 5) and ApoE$^{-/-}$Irgm1$^{+/-}$ (n = 3) bone marrow chimera recipient mice; scale bars = 200 μm. (I, J) Quantitative analyses of the percentage of neutral lipid and collagen content in the plaques, respectively. (K-L) Representative images(K) and quantitative analyze(L) of cleaved-caspase3 in aortic sinus plaques. NC=negative control; scale bars = 100 μm. (M) Western blotting was used to detect the cleaved-caspase3 and cleaved-caspase9 protein levels of the aortic arch from ApoE$^{-/-}$Irgm1$^{+/+}$ (n = 5) and ApoE$^{-/-}$Irgm1$^{+/-}$ (n = 3) bone marrow chimera recipient mice . GAPDH was used as a loading control. (N) Quantitative data represent the fold

change after normalized to GAPDH. ApoE$^{-/-}$Irgm1$^{+/+}$ vs. ApoE$^{-/-}$Irgm1$^{+/-}$, *$p < 0.05$, **$p < 0.01$. Results are presented as the mean ± SD. Statistical analysis: unpaired Student's *t-test*.

Figure 7. Summary of the role of IRGM/Irgm1 in atherosclerotic plaque progression by promoting macrophage apoptosis.

During the progression of atherosclerotic plaque, ox-LDL is continuously engulfed by the increasing number of macrophages. The expression of IRGM/Irgm1 in macrophages increases rapidly, which promotes the production of ROS, activates the MAPK signaling pathway, and finally induces macrophage apoptosis. The stability of the plaque then changes, with increases in the content of necrotic core, lipid, and cholesterol crystals, fibrous cap thinning, and a decrease in collagen fibers, transforming the plaque from stable to vulnerable. A vicious circle leads to further plaque progression and eventual plaque rupture.

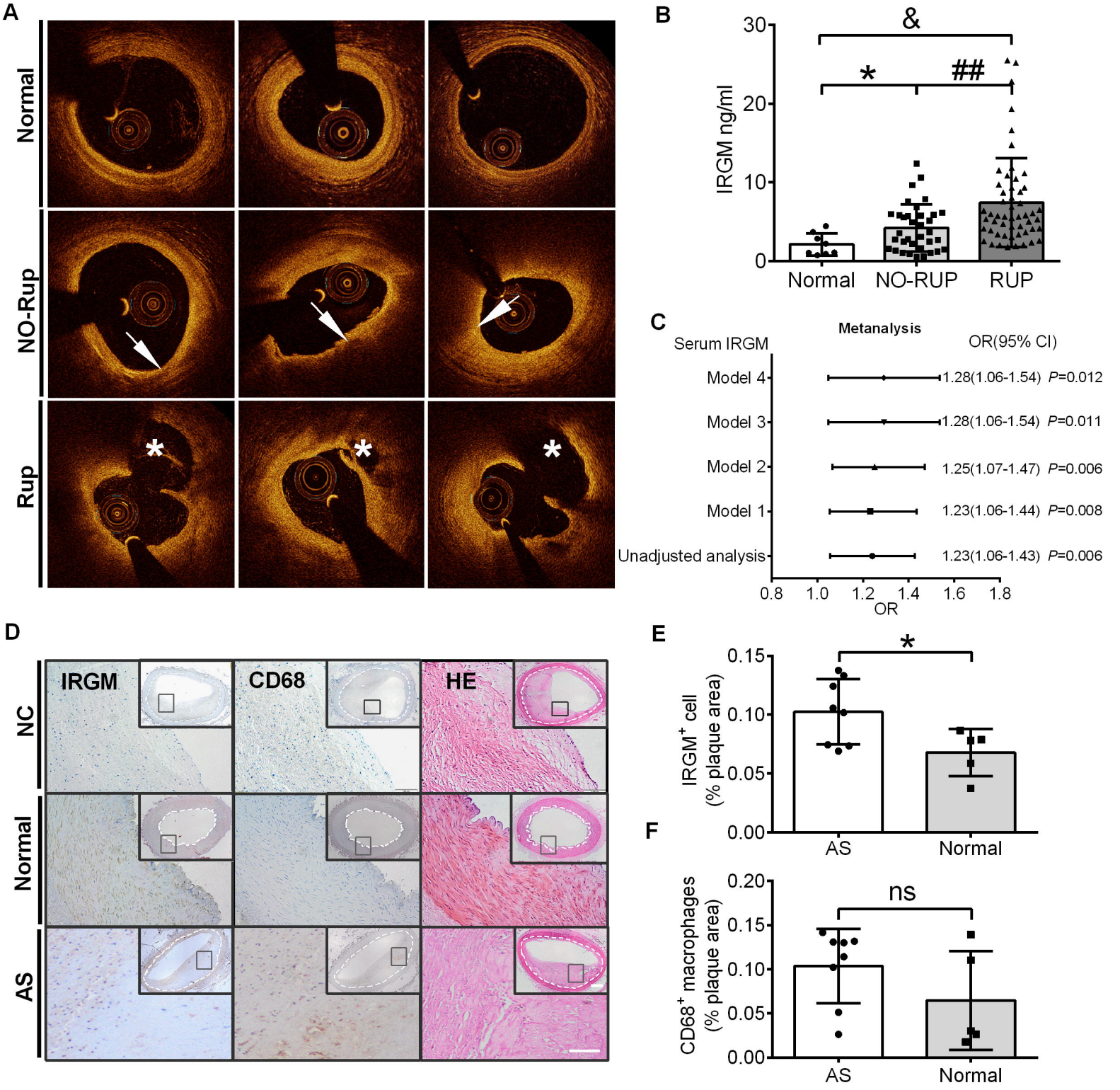
A
Normal
NO-Rup
Rup
B
IRGM ng/ml
30
20
10
0
&
*
##
Normal
NO-RUP
RUP
C
Metanalysis
Serum IRGM
OR(95% CI)
Model 4
1.28(1.06-1.54) P=0.012
Model 3
1.28(1.06-1.54) P=0.011
Model 2
1.25(1.07-1.47) P=0.006
Model 1
1.23(1.06-1.44) P=0.008
Unadjusted analysis
1.23(1.06-1.43) P=0.006
0.8
1.0
1.2
1.4
1.6
1.8
OR
D
IRGM
CD68
HE
NC
Normal
AS
E
IRGM+ cell (% plaque area)
0.15
0.10
0.05
0.00
*
AS
Normal
F
CD68+ macrophages (% plaque area)
0.20
0.15
0.10
0.05
0.00
ns
AS
Normal

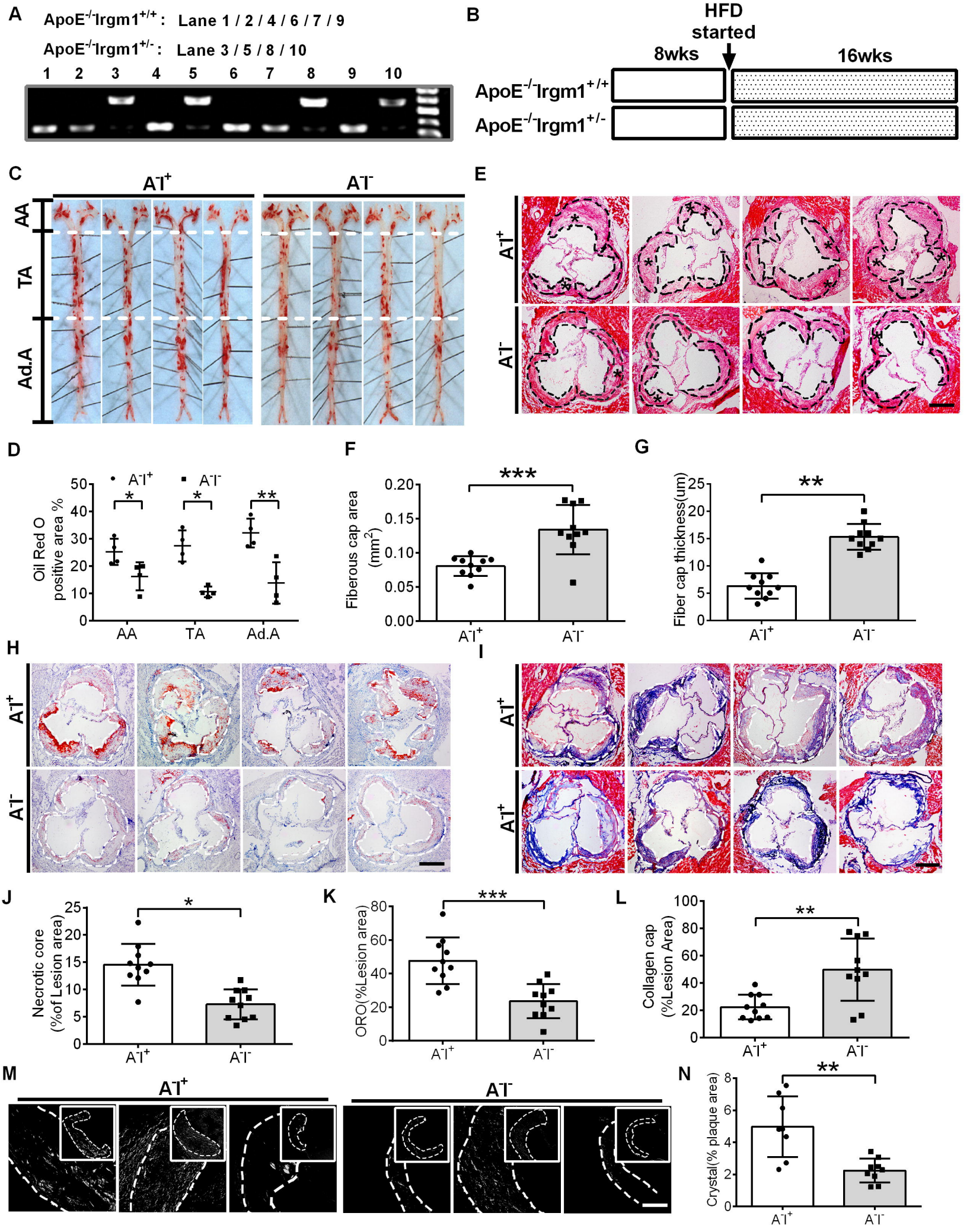
A
ApoE-/-Irgm1+/+ : Lane 1 / 2 / 4 / 6 / 7 / 9
ApoE-/-Irgm1+/- : Lane 3 / 5 / 8 / 10
1 2 3 4 5 6 7 8 9 10
B
HFD started
8wks
16wks
ApoE-/-Irgm1+/+
ApoE-/-Irgm1+/-
C
A-I+
A-I-
AA
TA
Ad.A
E
A-I+
A-I-
D
A-I+
A-I-
Oil Red O positive area %
AA
TA
Ad.A
F
Fiberous cap area (mm2)
A-I+
A-I-
G
Fiber cap thickness(um)
A-I+
A-I-
H
A-I+
A-I-
I
A-I+
A-I-
J
Necrotic core (%of Lesion area)
A-I+
A-I-
K
ORO(%Lesion area)
A-I+
A-I-
L
Collagen cap (%Lesion Area)
A-I+
A-I-
M
A-I+
A-I-
N
Crystal(% plaque area)
A-I+
A-I-

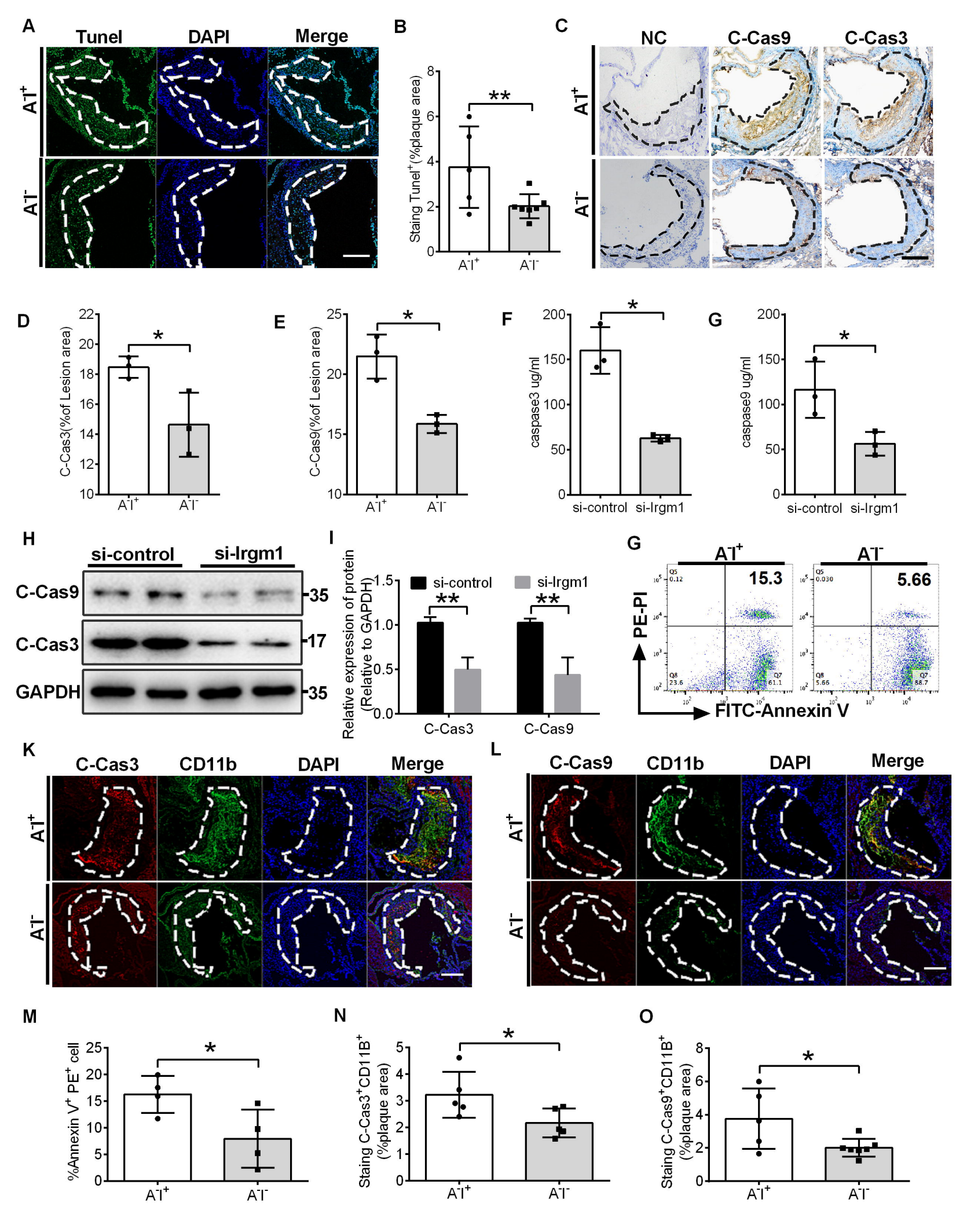
A
Tunel
DAPI
Merge
A-I+
A-I-
B
Staing Tunel+(%plaque area)
**
C
NC
C-Cas9
C-Cas3
D
C-Cas3(%of Lesion area)
*
E
C-Cas9(%of Lesion area)
F
caspase3 ug/ml
si-control
si-lrgm1
G
caspase9 ug/ml
H
si-control
si-lrgm1
C-Cas9
C-Cas3
GAPDH
35
17
I
Relative expression of protein (Relative to GAPDH)
si-control
si-lrgm1
C-Cas3
C-Cas9
G
15.3
5.66
PE-PI
FITC-Annexin V
K
C-Cas3
CD11b
DAPI
Merge
L
C-Cas9
M
%Annexin V+ PE+ cell
N
Staing C-Cas3+CD11B+ (%plaque area)
O
Staing C-Cas9+CD11B+ (%plaque area)

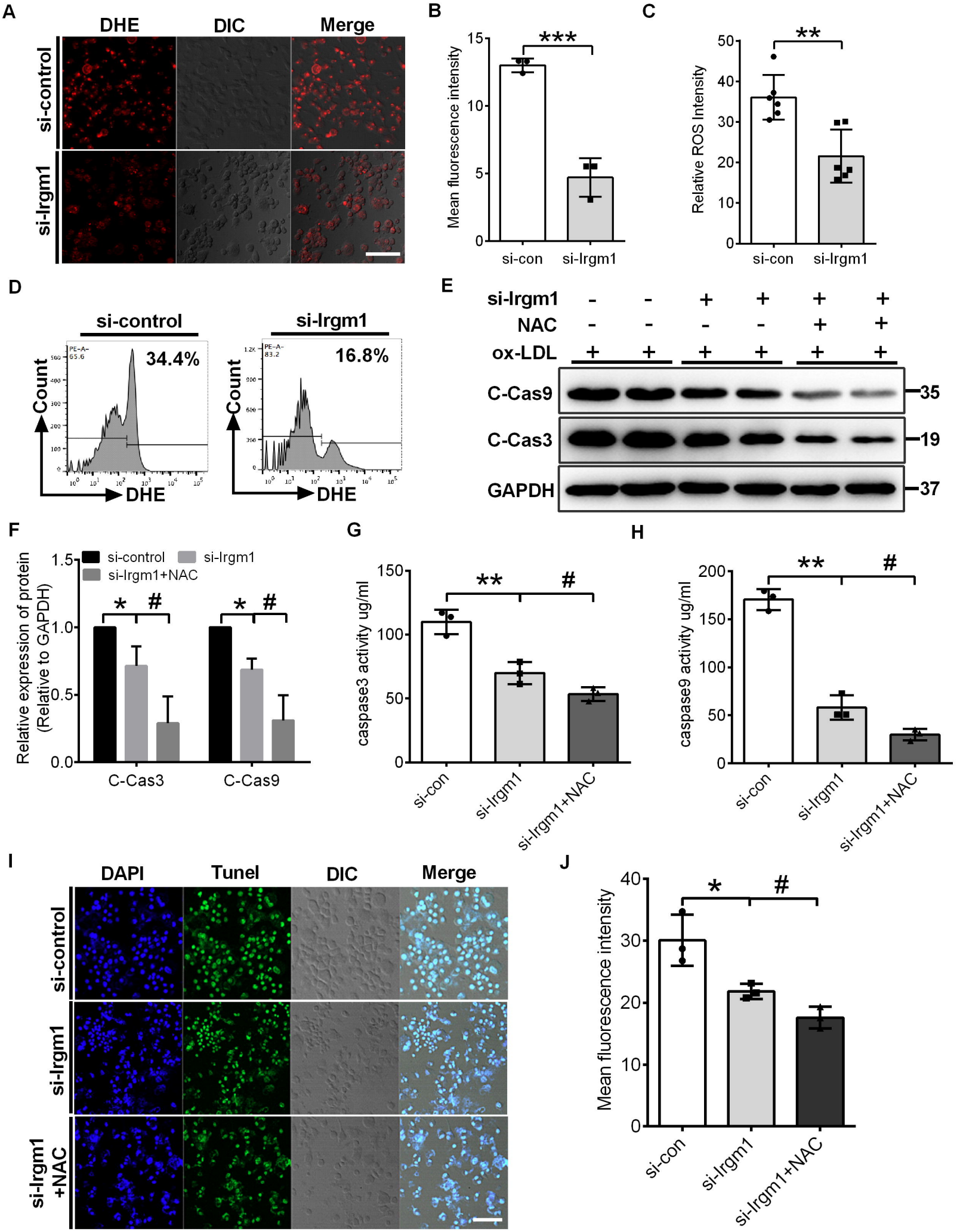
A
DHE
DIC
Merge
si-control
si-lrgm1
B
Mean fluorescence intensity
***
si-con
si-lrgm1
C
Relative ROS Intensity
**
si-con
si-lrgm1
D
si-control
si-lrgm1
34.4%
16.8%
Count
DHE
E
si-lrgm1
NAC
ox-LDL
C-Cas9
C-Cas3
GAPDH
35
19
37
F
si-control
si-lrgm1
si-lrgm1+NAC
Relative expression of protein (Relative to GAPDH)
C-Cas3
C-Cas9
G
caspase3 activity ug/ml
si-con
si-lrgm1
si-lrgm1+NAC
H
caspase9 activity ug/ml
si-con
si-lrgm1
si-lrgm1+NAC
I
DAPI
Tunel
DIC
Merge
si-control
si-lrgm1
si-lrgm1 +NAC
J
Mean fluorescence intensity
si-con
si-lrgm1
si-lrgm1+NAC

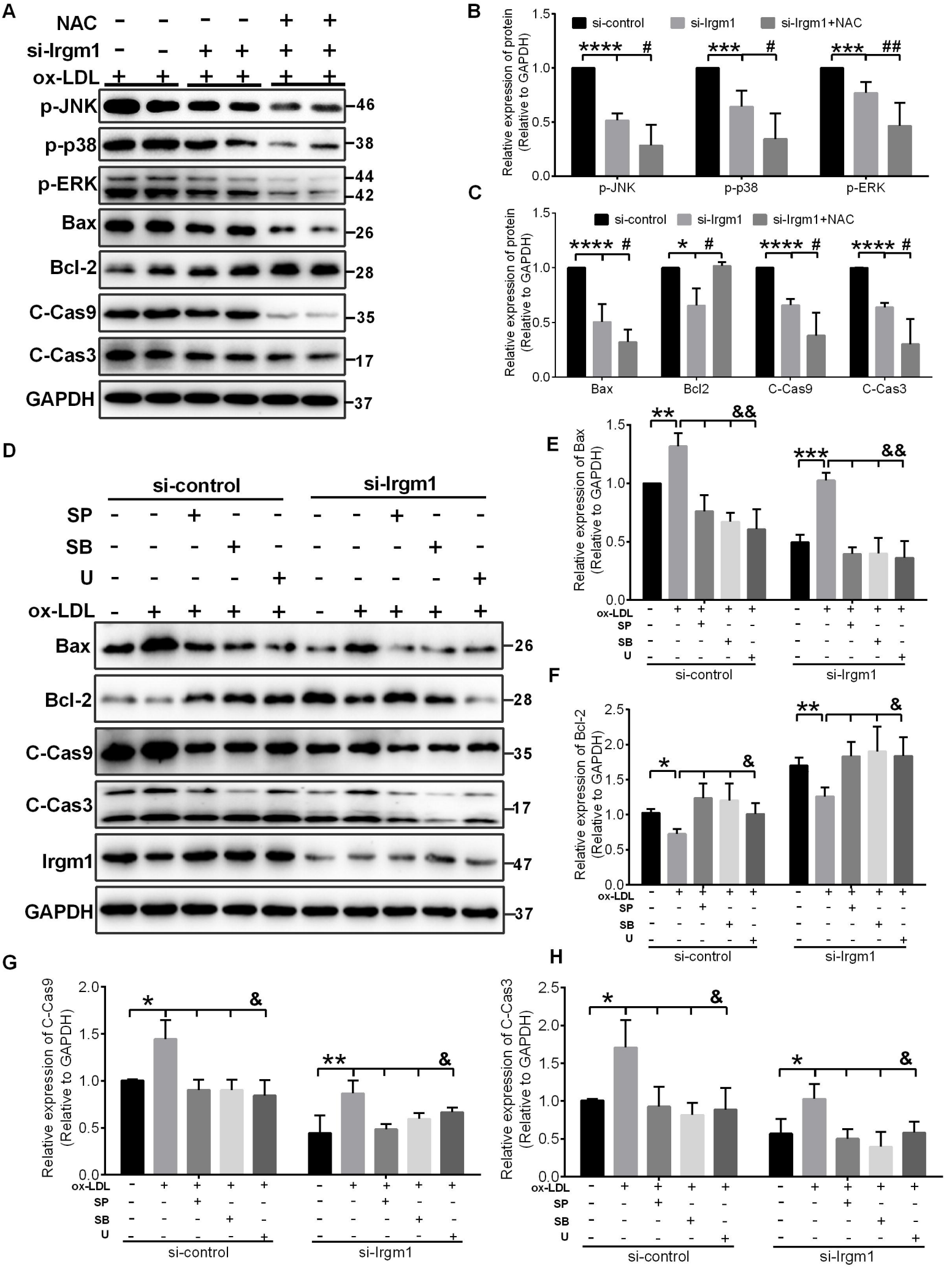
A
NAC
si-Irgm1
ox-LDL
p-JNK
p-p38
p-ERK
Bax
Bcl-2
C-Cas9
C-Cas3
GAPDH
46
38
44
42
26
28
35
17
37
B
si-control
si-Irgm1
si-Irgm1+NAC
Relative expression of protein (Relative to GAPDH)
p-JNK
p-p38
p-ERK
C
Bax
Bcl2
C-Cas9
C-Cas3
D
si-control
si-Irgm1
SP
SB
U
ox-LDL
Irgm1
E
Relative expression of Bax (Relative to GAPDH)
F
Relative expression of Bcl-2 (Relative to GAPDH)
G
Relative expression of C-Cas9 (Relative to GAPDH)
H
Relative expression of C-Cas3 (Relative to GAPDH)

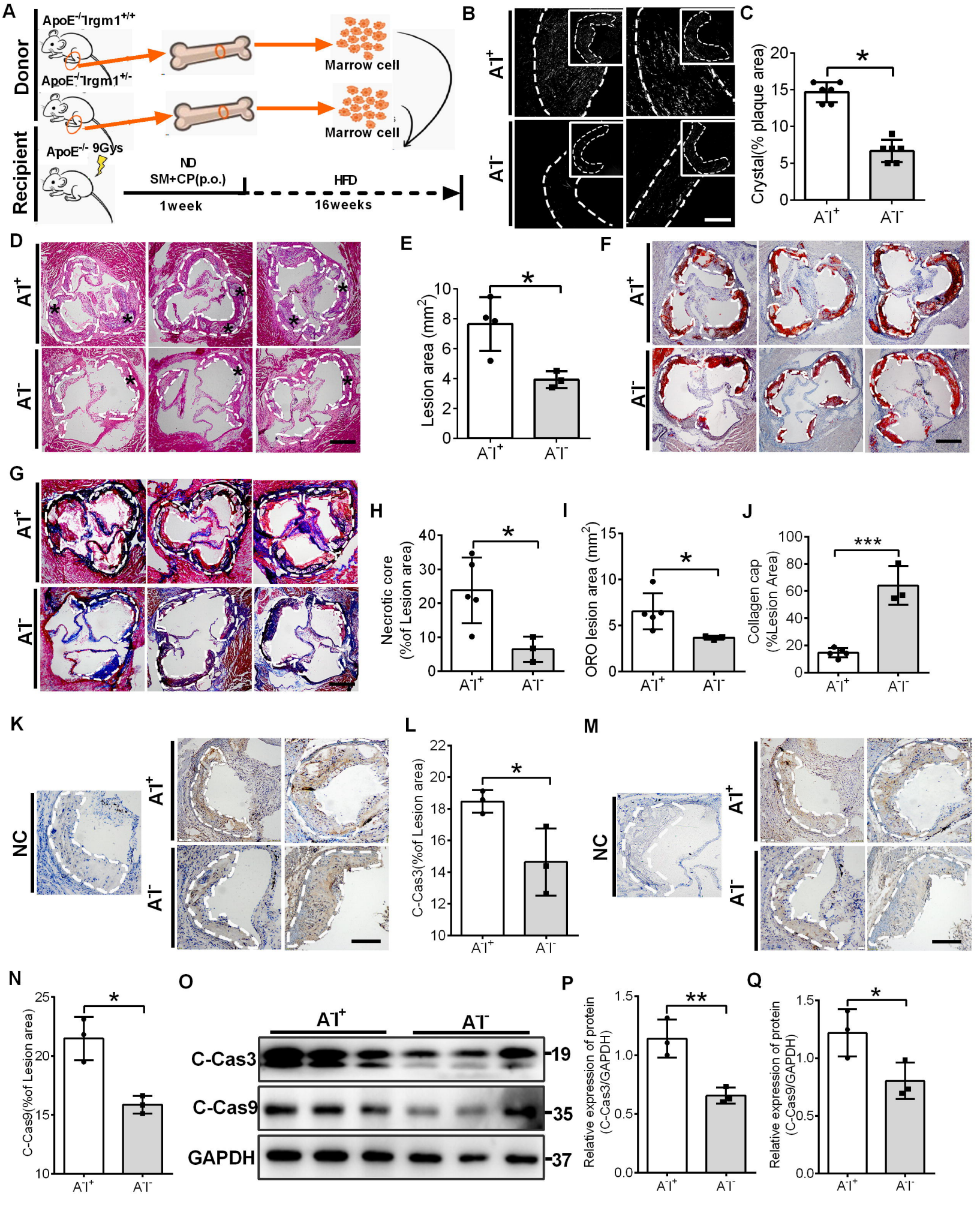
A
Donor
Recipient
ApoE-/-Irgm1+/+
ApoE-/-Irgm1+/-
ApoE-/- 9Gys
Marrow cell
Marrow cell
ND
SM+CP(p.o.)
1week
HFD
16weeks
B
A-I+
A-I-
C
Crystal(% plaque area)
D
E
Lesion area (mm2)
F
G
H
Necrotic core (%of Lesion area)
I
ORO lesion area (mm2)
J
Collagen cap (%Lesion Area)
K
NC
L
C-Cas3(%of Lesion area)
M
N
C-Cas9(%of Lesion area)
O
C-Cas3
C-Cas9
GAPDH
19
35
37
P
Relative expression of protein (C-Cas3/GAPDH)
Q
Relative expression of protein (C-Cas9/GAPDH)

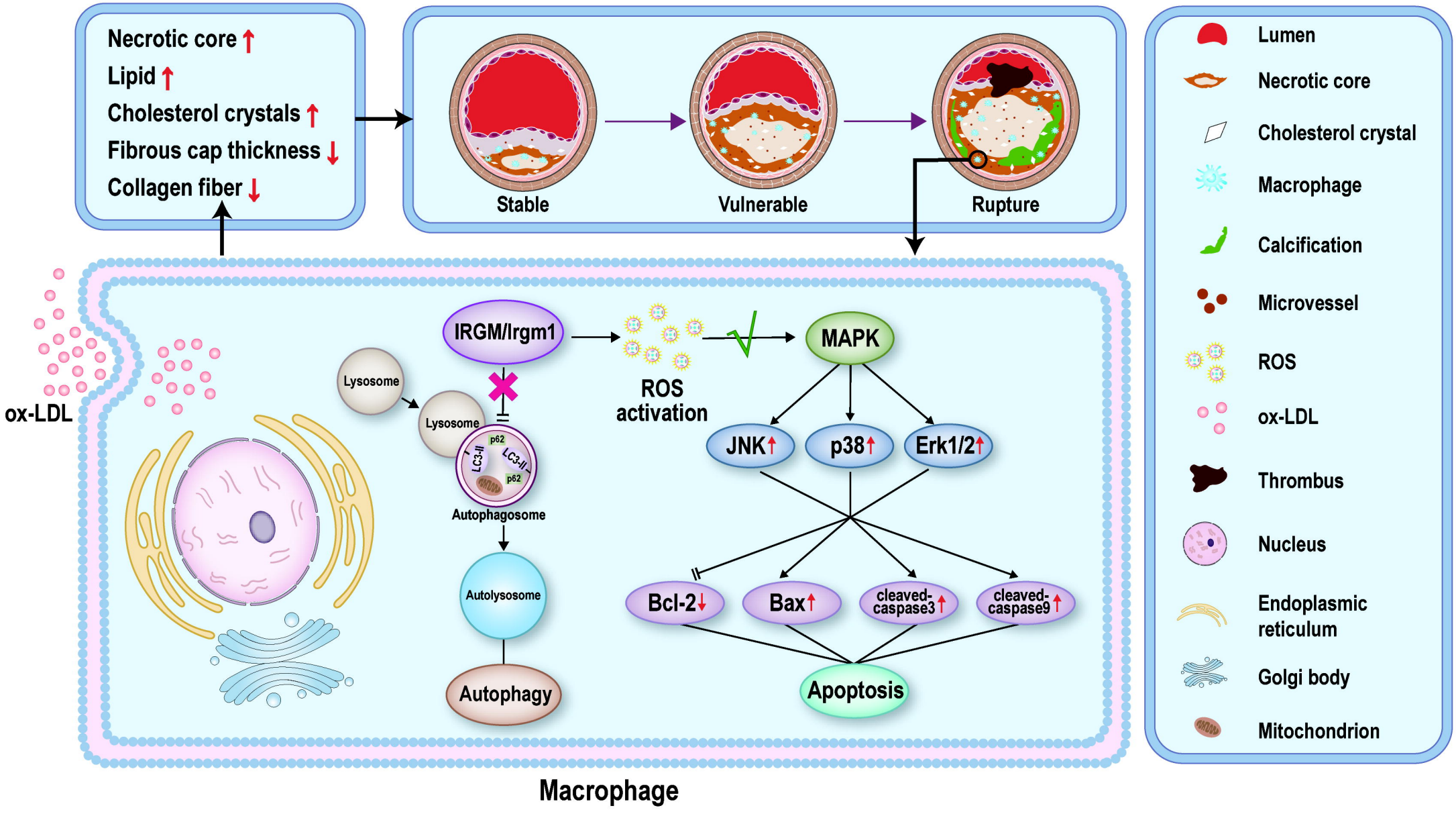
Necrotic core ↑
Lipid ↑
Cholesterol crystals ↑
Fibrous cap thickness ↓
Collagen fiber ↓
Stable
Vulnerable
Rupture
ox-LDL
IRGM/Irgm1
Lysosome
Lysosome
p62
LC3-I
LC3-II
p62
Autophagosome
Autolysosome
Autophagy
ROS
activation
MAPK
JNK↑
p38↑
Erk1/2↑
Bcl-2↓
Bax↑
cleaved-caspase3↑
cleaved-caspase9↑
Apoptosis
Macrophage
Lumen
Necrotic core
Cholesterol crystal
Macrophage
Calcification
Microvessel
ROS
ox-LDL
Thrombus
Nucleus
Endoplasmic reticulum
Golgi body
Mitochondrion